Journal of Power Sources 248 (2014) 427–433

Contents lists available at ScienceDirect

Journal of Power Sources

journal homepage: www.elsevier.com/locate/jpowsour

Soybean-derived mesoporous carbon as an effective catalyst support for electrooxidation of methanol

Tianbao Zhou [a], Hui Wang [a], Shan Ji [b], Vladimir Linkov [b], Rongfang Wang [a,*]

[a] Key Laboratory of Eco-Environment-Related Polymer Materials, Ministry of Education of China, College of Chemistry and Chemical Engineering, Northwest Normal University, Lanzhou 730070, China
[b] South African Institute for Advanced Materials Chemistry, University of the Western Cape, Private Bag X17, Bellville 7535, Cape Town, South Africa

HIGHLIGHTS

- A mesoporous support derived soybean, e.g. CS, was prepared.
- Pt nano sized dendrites were dispersed on the surface of CS.
- Pt/CS has high catalytic activity for CO and methanol oxidation.

GRAPHICAL ABSTRACT

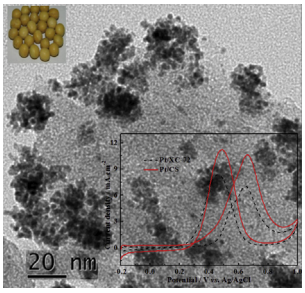

ARTICLE INFO

Article history:
Received 14 June 2013
Received in revised form
25 September 2013
Accepted 25 September 2013
Available online 4 October 2013

Keywords:
Electrocatalysts
Support
Soybean
Methanol oxidation
Fuel cell

ABSTRACT

In this work, a low cost and nitrogen-containing carbon (CS) with mesoporous structure and high surface area is synthesized by carbonizing soybean. It is found that the prepared CS has excellent textural properties such as high specific surface areas and large pore diameters. TEM images show that the Pt nano-sized dendrites are well formed on the surface of CS. Compared to Pt supported on Vulcan carbon XC-72, electrochemical results show that Pt supported on CS possesses a higher electrocatalytic activity and better durability in methanol oxidation reaction, which are mainly attributed to the support effect of CS resulting in the unique morphology of Pt particles and high content of Pt(0). These results indicate that CS has great potential as a high-performance catalyst support for fuel cell electrocatalysis.

1. Introduction

Due to their high efficiency and low emissions, low-temperature fuel cells (LTFCs) are attracting considerable interest as a means of direct electrochemical conversion of chemical energy into electricity, which are considered to be a promising power sources for transportation, stationary and portable applications [1–4]. Despite these advantages, low durability and high cost of platinum (Pt-) based catalysts still limit their practical applications [5,6]. Research efforts have been focused on decreasing the cost of Pt-based catalysts by three main approaches (i) reducing Pt loading; (ii) exploring low cost alternative to Pt and (iii) developing new support to replace conventional carbon black [5,7–10]. Currently, carbon black, i.e. Vulcan XC-72, is the state-of-the-art support materials, which dominates as support material for catalysts used in LTFCs. Although carbon black has high surface area and good electric conductivity, it is not satisfactory due to its high cost and

* Corresponding author.
E-mail addresses: sji@uwc.ac.za (S. Ji), wrf38745779@126.com, wangrf@nwnu.edu.cn (R. Wang).

0378-7753/$ – see front matter © 2013 Elsevier B.V. All rights reserved.
http://dx.doi.org/10.1016/j.jpowsour.2013.09.108

the weak interaction between carbon black and Pt nanoparticles, which results in aggregation of Pt nanoparticles and further reducing the Pt active surface [11]. Recently, developing nitrogen doped carbon supports have received considerable attentions as a new family of highly efficient support for fuel cells [8,12].

There are a plenty of studies proving that the physical and electrochemical properties of carbon supports can be significantly improved by doping heteroatoms, especially nitrogen [13–15]. Abundant free π electrons are available in the carbon, which make it a potential material as catalyst, but these π electrons are inert for chemical reactions. It was found that the carbon π electrons can be activated by conjugating with lone-pair electrons from N dopants [16]. Nitrogen doping can also introduce chemically active site onto the surface of carbon supports which act as anchoring site for metal nanoparticle deposited on its surface [17]. In addition, mesoporous carbon can also improve the electrocatalytic performance by enhancing three phase boundary, forming high and uniform dispersion of metal nanoparticles and enhancing the electron transfer [18,19]. It is expected that to combine improved electrocatalytic properties of N-doped carbon with mesoporous structures with good electronic conductivity could result in a good support for LTFCs, which can boost the catalytic performance and stability via well-dispersed Pt nanoparticles, stronger linkage between Pt and support, and meso-porosity.

In this work, a facile and environmental friendly method has been developed to produce mesoporous N-doped carbon via carbonizing soybeans (as shown in Fig. 1). Soybean is a cheap material as it is a naturally abundant and sustainable source with high molecular weight and nitrogen content. The nitrogen content in soybeans is ca. 6%, which make it a promising material for preparing N-doped carbon. Because of above reasons, we decided to prepare nitrogen-doped carbon materials using soybean. A mesoporous N-doped carbon support was successfully prepared by this method. Subsequently, Pt nanoparticles were deposited onto the synthesized nitrogen-doped carbon support and its morphology and electrocatalytic properties were also investigated.

2. Experimental

2.1. Carbonization of soybeans

Carbonization of soybeans was carried out as follows: soybeans purchased on local market (see Fig. 1a) were dehydrated in an oven and ball-milled for 6 h. 10 g of ball-milled soybean powder (see Fig. 1b) was placed in a quartz tube furnace and then heated to 800 °C with a heating rate of 5 °C min^{-1} under N_2 atmosphere and then kept at 800 °C for 2 h. After the furnace cooled to room temperature, a black powder (see Fig. 1c) was obtained. The obtained powder was ball-milled for 4 h, and then immersed into acetone and kept at 60 °C for 2 h. After that, the suspension was filtered, washed with deionized water and then dried at 60 °C. After the treatment of acetone, the black powder was added to 2 mol L^{-1} HNO_3 solution with 3% H_2O_2, and stirred at room temperature for 24 h. The black powder was recovered by filtering and washing, and then dried at 60 °C for 12 h. The obtained powder was placed in tube furnace again and heated to 800 °C for another 2 h. When the tube furnace cooled to room temperature, the black powder was treated with 2 mol L^{-1} HNO_3 solution with 3% H_2O_2 again. Subsequently, the black powder was rinsed and dried at 60 °C for 12 h. The resulting black powder was labeled as carbonized soybean (CS).

2.2. Preparation of Pt/CS

Pt/CS was synthesized by a modified organic colloid method in an ethylene glycol (EG) solution as described below: 3.3 mL of 20 mg mL^{-1} H_2PtCl_6 was used as received and dissolved in 30 mL EG + 15 mL deionized water. Subsequently, 33.3 mg potassium acid phthalate and 100 mg CS were added into the above solution with vigorous stirring. The pH of the mixture solution was adjusted to ~9 by adding 5 wt.% of KOH/EG solution, and then sonicated for 40 min. After that, $NaBH_4$ solution (80 mg $NaBH_4$ dissolved in EG solution) was dropwise added to above solution and stirred for 25 h. The resulting powder was collected by filtration, rinsed with ultrapure water 10 times and dried overnight in a vacuum oven at 100 °C. For comparison purposes, Pt nanoparticles deposited on Vulcan carbon XC-72 (Pt/XC-72) were synthesized by the same procedure of synthesizing Pt/CS.

2.3. Physical characterizations

Elemental Analysis was measured by organic elemental analyzer (Thermo Flash2000). The specific surface area was determined by Brunauer–Emmett–Teller (BET) method and the pore size distribution was calculated by the density functional theory (DFT) method using the model (slit pore, NLDFT equilibrium model) on Quantachrome Autosorb-1 volumetric analyzer. X-ray diffraction (XRD) patterns of the catalysts were characterized on a Shimadzu XD-3A (Japan) goniometer, using Cu Kα radiation operated at 40 kV and 35 mA at room temperature. X-Ray Photoelectron Spectroscopy (XPS) spectra were generated by using a PHI-5702 multifunctional X-ray photoelectron spectrometer (American) respectively. Scanning electron microscopy (SEM) images were conducted on Carl Zeiss Ultra Plus. Transmission electron microscopy (TEM) measurements were carried out using a JEM-2010 Electron Microscope (Japan) with an acceleration voltage of 200 kV. The chemical composition of the samples was determined using the energy dispersive X-ray analysis (EDS) technique coupled to TEM. Raman spectroscopy was carried out on a FT-Raman

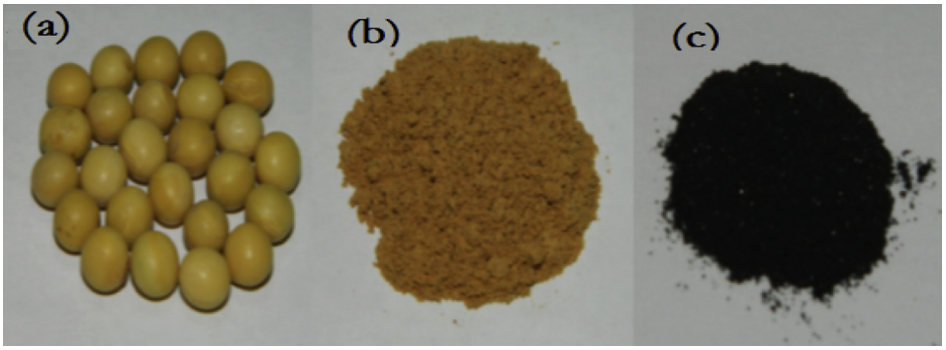

Fig. 1. Macroscopic changes from soybeans (a), soybean powder (b) to CS (c).

spectroscopy (RFS 100, BRUKER) employing Nd:YAG laser wavelength of 1064 nm.

2.4. The electrochemical characterizations

The electrochemical measurements of catalysts were performed on an Autolab electrochemical work station (PGSTAT128N, Eco Chemie, Netherlands). A conventional three-electrode electrochemical cell was used for the measurements, including a platinum wire as the counter electrode, an Ag/AgCl (saturated KCl solution) electrode as the reference electrode, and a glass carbon electrode (5 mm in diameter) as the working electrode. The thin film electrode was prepared as follows: 5 mg of catalyst was dispersed ultrasonically in 1 mL of Nafion/ethanol (0.25% Nafion). About 8 μL of the dispersion was transferred onto the glassy carbon disc using a pipette, and then dried in the air to form catalyst layer on it. Before each measurement, the solution was purged with high-purity N_2 (for oxygen-free solutions) for at least 30 min.

3. Results and discussion

First of all, the practical composition of CS was evaluated by elemental analysis. The analytical results indicate that CS consists of N (7.1 wt.%), C (51.2 wt.%), H (7.2 wt.%), S (0.10 wt.%) and the reminder inorganic salt residue. Fig. 2 shows adsorption–desorption isotherms of N_2 at 77 K for CS. The isotherms of the sample belong to Langmuir I at low relative pressures (P/P_0) and type IV at intermediate and high relative pressures. The initial part of the N_2 isotherm for CS represents micropore fillings, and the slope of the plateau at high relative pressure is assigned to multilayer adsorption in the mesopores, or macropores and on the external surface [20]. As shown in Fig. 2, hysteresis behavior is observed in the N_2 adsorption–desorption isotherms due to the presence of ink-bottle type of pores in CS [21]. According to the Kelvin equation [22], hysteresis behavior represents that the sample has a large pore size since hysteresis occurs at high relative pressure. Based on the N_2 sorption data, the BET surface area and total pore volume for the prepared CS are determined to be 516.6 $m^2\ g^{-1}$ and 0.45 $cm^3\ g^{-1}$, respectively. The BET surface area of XC-72 is 245 $m^2\ g^{-1}$ determined in our previous work [23]. These results indicate CS has larger BET surface area than Vulcan carbon, which would be conducive to the process of mass transfer. The pore size distributions of CS was shown as the inset of Fig. 2. It can be observed CS exhibits the pore size distributions in the range between ca. 1.5 and 36 nm. There are no peaks in the micropore range. While, a significant peak centering at ca. 3.8 nm is presented in the mesopore range, in which other relatively weak peaks can also be observed. These findings suggest that CS has mesopores structure.

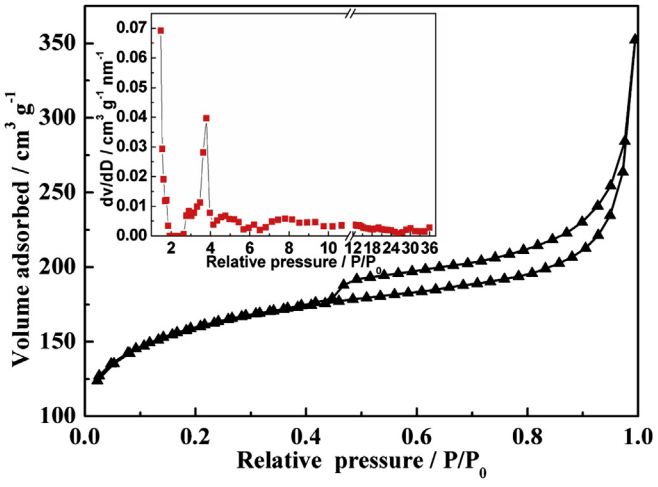

Fig. 2. N_2 adsorption–desorption isotherms of CS; inset: pore size distribution of CS.

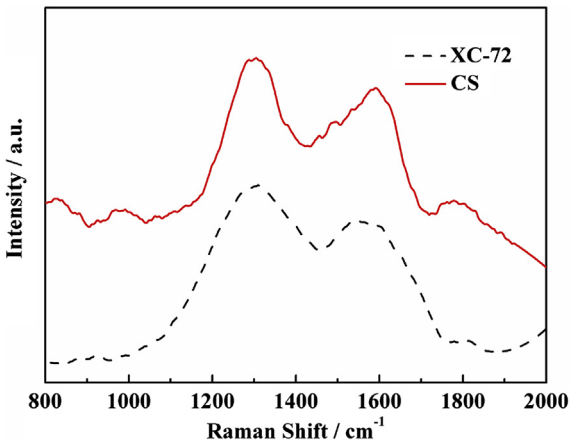

Fig. 3. Raman spectra of XC-72 and CS.

Raman spectroscopy was carried out to investigate the chemical structure and the degree of structure defect of CS and XC-72 (as shown in Fig. 3). Raman spectra of CS and XC-72 show two peaks at about 1300 and 1580 cm^{-1}, which is the Raman active D-band and Raman active G-band, respectively [24]. The D-band becomes active because of a reduction of symmetry near or at the crystalline edges, which is ascribed to the finite-sized crystals of graphite. G-band is attributed to all sp^2 bonds of graphitic network [25]. The ratio of the relative intensities of D-band and G-band (I_D/I_G) can be used to measure the defects on the sample. A higher I_D/I_G indicates more defects existed on the support [26]. By measuring the Raman spectra, the I_D/I_G of CS and carbon is 1.13 and 1.26, respectively. The I_D/I_G of CS is lower than that of carbon, which indicated that the defects on CS is lower than XC-72. It was expected that introducing N atoms into carbon will result in an increase in D-band. However, in some case, the intensity of D-band doesn't increase with the nitrogen content [27]. Currently, there is still no clear explanation for this phenomenon. Ghosh et al. [27] explained that perhaps N-dopants are more utilized in creating internal compartment rather than forming surface distortion. Compared with Raman spectrum of carbon, there is a clear downshift of D-band for CS. For CS sample, downshift of D-band and relative low I_D/I_G are obvious evidences that electronic structure of carbon layers is changed.

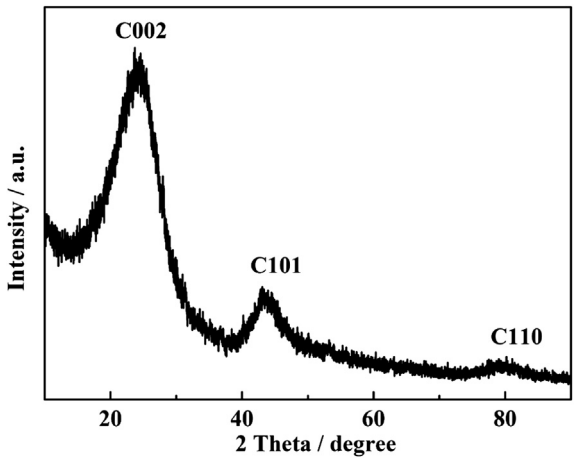

Fig. 4. XRD pattern of CS.

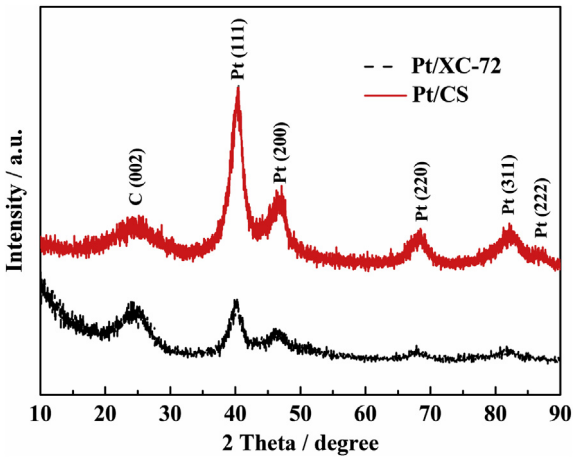

Fig. 5. XRD patterns of Pt/CS and Pt/XC-72.

The XRD pattern of carbonized soybean is shown in Fig. 4. In the XRD pattern of CS, there are three diffraction peaks at 26°, 42° and 79°, which are attributed to the hexagonal graphite structures, i.e. (002), (101) and (110) planes, respectively [28]. However, all three diffraction peaks are broad and weak, which indicate graphite with amorphous structure was formed after the soybeans was carbonized and acid-treated.

Fig. 5 shows the XRD patterns of Pt/CS and Pt/XC-72. Both of samples have peaks at 39.5°, 46°, 67° and 81.5°, which are the characteristic peaks of face centered cubic (fcc) crystalline Pt (111), (200), (220) and (311) plane [29], respectively. Accordingly, the average Pt particle sizes for Pt/CS and Pt/XC-72 can be calculated by the Scherrer formula [30], which are 3.4 and 3.1 nm, respectively.

Fig. 6a displays SEM image of as-prepared CS. It can be observed that CS shows irregular shape with the size from tens of nanometers to several microns. Fig. 6b and c shows TEM images of Pt nanoparticles deposited on CS support at different magnification and its corresponding EDS. The Pt nanoparticles formed on CS support are different from the Pt nanoparticles usually formed on the conventional carbon support. Pt nano sized dendrites were formed on the surface of CS, which are similar to the Pt nanodendrites reported by Xia's group [31]. It was reported that Pt nanoparticle with dendrite structure were two and a half times more active on the basis of equivalent Pt mass than Pt/C. These Pt dendritic particles on CS have an average particles size of 20 nm, in which there are many small Pt nanoparticles. The EDS results show that there are Pt, N, O and C existed in this catalyst. When Vulcan carbon was used as the support, the morphology of Pt deposited is irregular round particles which are uniformly dispersed. Comparison of TEM images between Pt/CS and Pt/XC-72 shows that the different supports result in the different disperse of metal particles.

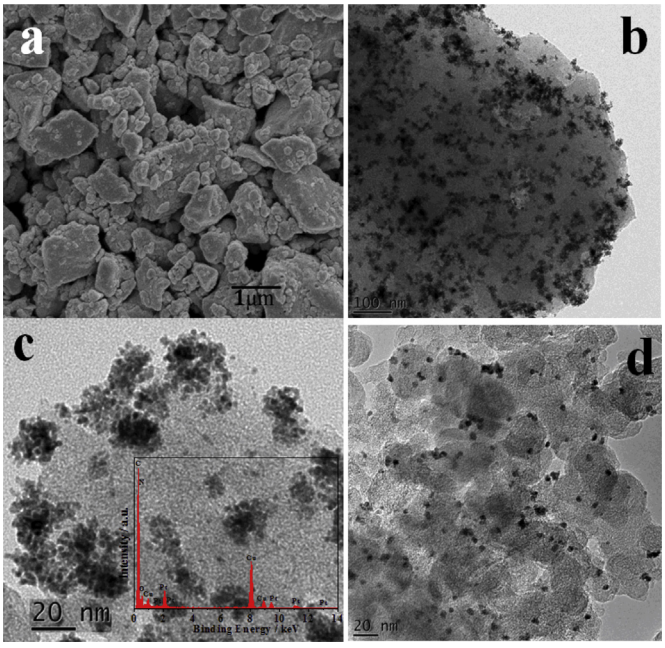

Fig. 6. (a) SEM image of CS; (b and c) TEM images with different magnifications and inset in figure c: EDS pattern of Pt/CS; (d) TEM image of Pt/XC-72.

XPS is an efficient way to study the surface oxidation states. As shown in Fig. 7, the Pt 4*f* binding energy region of Pt/CS and Pt/XC-72. The Pt 4*f* XPS spectra consists of two peaks corresponding to Pt $4f_{7/2}$ and Pt $4f_{5/2}$ states from spin–orbital splitting. The Pt 4*f* spectra were deconvoluted into three doublets which correspond to different oxidation states of Pt, i.e. Pt(0), Pt(II) and Pt(IV) [32]. Compared with the XPS of Pt/XC-72, there is a clear shift to higher energy region of the Pt 4*f* peak in the XPS spectrum of Pt/CS due to the interaction between Pt and support resulting in electron-rich Pt [33]. Comparison of binding energies of Pt $4f_{7/2}$ and Pt $4f_{5/2}$ between Pt/CS and Pt/XC-72 is presented in Table 1. Since the intensities of these XPS peaks are related to the amount of Pt species, the amounts of different oxidation states of Pt can be calculated from the relative intensities of these peaks. As shown in Table 1, it can be seen that there is a high content metallic Pt in Pt nanoparticles formed using CS as the support.

It has been reported that there are four types of nitrogen species in the carbon-based materials, such as coal and char [34]. The four types of nitrogen in the carbon-based materials are in the form of pyridinic-N (398.6 ± 0.3 eV), pyrrolic-N (400.5 ± 0.3 eV), quaternary nitrogen (401.3 ± 0.3 eV) and pyridinic N^+-O^- (402–405 eV). As shown in Fig. 8, there are three peaks in the N1s spectra for Pt/CS, corresponding to pyridinic-N (N_1), pyrrolic-N (N_2) and quaternary nitrogen (N_3). Pyridinic-N can provide one *p*-electron to the aromatic π-systems which has a pair of electron in the plane of the carbon matrix, so pyridinic-N can increase electron-donor property of the catalyst. Usually, presence of pyridinic-N in the support led to a higher enhancement of electrochemical performance [35].

Fig. 9 shows the cyclic voltammograms (CV) of Pt/XC-72 and Pt/CS electrocatalysts in 0.5 mol L^{-1} H_2SO_4 electrolyte between −0.2 and +1.0 V (*vs.* Ag/AgCl) at a scan rate of 50 mV s^{-1}. The characteristic peaks of polycrystalline Pt, i.e. hydrogen adsorption/desorption peaks in low potential region, oxide formation/stripping wave/peak in high potential region and a flat double layer in between, are observed for both produced catalysts. The two peaks (between −0.1 and 0.0 V) of hydrogen desorption are clearly shown in the CV of both Pt/CS and Pt/XC-72. These two peaks at −0.1 and 0.0 V (*vs.* Ag/AgCl) are mainly attributed to the electrocatalytic reactions occurring on the Pt (111) and Pt (100) planes, respectively [36]. In addition, the double current layer is visibly broader for Pt/CS than Pt/C, implying that Pt/CS has a significantly larger electrochemically accessible area than Pt/C [37].

CO stripping voltammetry can be used to test the activity of a catalyst for electrochemically oxidizing the chemisorbed CO on the surface of catalysts. CO stripping voltammograms of Pt/CS and Pt/XC-72 in 0.5 mol L^{-1} H_2SO_4 solution at 50 mV s^{-1} at room temperature were presented in Fig. 10. A peak current attributed to CO oxidation is observed on both catalysts in the first scan and disappeared in the subsequent scan, which indicate that the adsorbed CO is completely oxidized in the first potential forward scan. The onset potential for the CO oxidation reaction on Pt/CS shifts to more

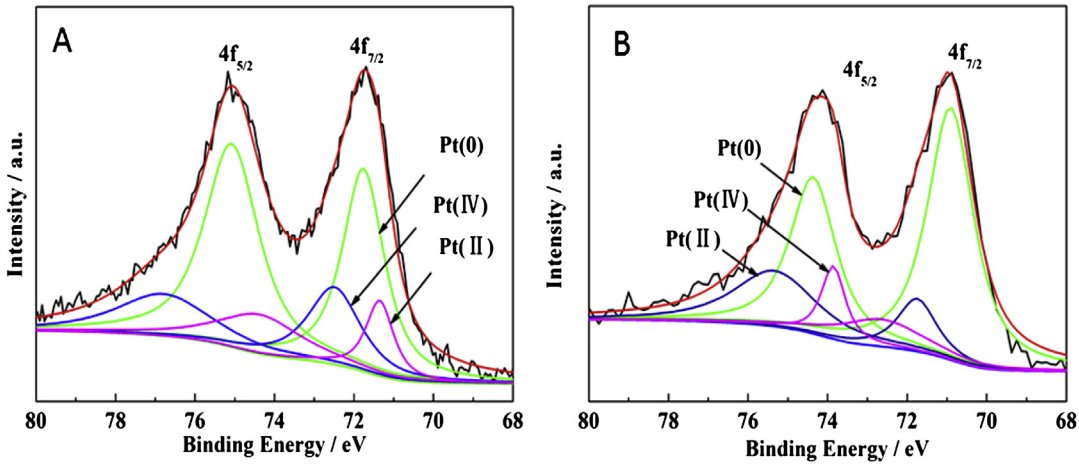

Fig. 7. Pt 4f XPS spectra of (A) Pt/CS and (B) Pt/XC-72.

negative side than Pt/XC-72, which means that Pt/CS is more active for CO oxidation reaction than Pt/XC-72. In addition, the peak of CO oxidation on Pt/CS is broader than that of Pt/XC-72, indicating that CO oxidation reaction on Pt/CS occurs in a larger voltage range.

The CVs of Pt/CS and Pt/XC-72 catalysts for methanol oxidation presented in Fig. 11 were obtained in N_2-saturated 0.5 mol L^{-1} CH_3OH + 0.5 mol L^{-1} H_2SO_4 solution at 50 mV s^{-1} at room temperature. As shown in Fig. 11, the onset potential of methanol oxidation of Pt/CS is 0.25 V (*vs.* Ag/AgCl), which is much lower than that of Pt/XC-72 catalyst, i.e. 0.35 V (*vs.* Ag/AgCl). There is 100 mV difference between the onset potentials of methanol oxidation on Pt/CS and Pt/XC-72, which indicates that methanol oxidation reaction is more likely to easy occur on Pt/CS. It is also found that the peak oxidation current of Pt/CS was 1.5 times higher than that of Pt/XC-72. As the previous XPS discussion, compared to Pt/XC-72, Pt/CS has the larger amount of metallic Pt, which would be contributed to more active sites towards the methanol oxidation, thus resulting in the enhanced catalytic activity. The ratio of positive scan peak current density (I_f) to negative scan peak current density (I_b) can be used to describe the catalyst tolerance to carbonaceous species. Higher ratio means higher tolerance to carbonaceous species on the surface of catalyst [10]. The I_f/I_b of Pt/CS is 0.95, which is higher than that of Pt/XC-72 (0.84). This result implies that Pt/CS catalyst has a better tolerance to CO than Pt/XC-72.

Fig. 12 shows the chronoamperometric curves of methanol oxidation in 0.5 mol L^{-1} CH_3OH + 0.5 mol L^{-1} H_2SO_4 solution at 0.6 V at room temperature on Pt/CS and Pt/XC-72 electrodes. When the potential is set at constant value, continuous methanol oxidation occurs on the surface of the catalyst. In this case, chemisorbed intermediates form and accumulate on the surface of catalyst and results in decay of catalytic activity. Chronoamperometric analysis usually indicates the rate of decay of the current density with time, which is directly linked with durability. The initial current density

Table 1
Binding energies and relative intensities of the different Pt species for Pt/CS and Pt/XC-72 catalysts.

Catalysts	Species	Binding energy of Pt $4f_{7/2}$/eV	Relative intensity %
Pt/XC-72	Pt^0	71.2	59.9
	Pt^{II}	72.3	24.0
	Pt^{IV}	73.7	16.1
Pt/CS	Pt^0	71.3	63.9
	Pt^{II}	72.5	22.3
	Pt^{IV}	73.8	13.8

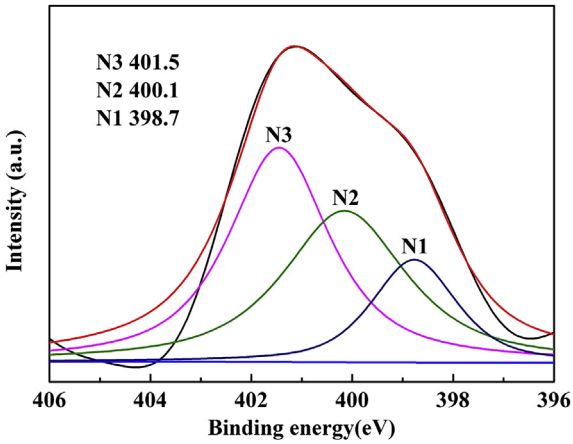

Fig. 8. N1s XPS spectrum of CS.

of Pt/CS is much higher than that of Pt/XC-72, whose active sites available on the surface of Pt/CS is more than that of Pt/XC-72. At 1000 s, the current densities of Pt/CS and Pt/XC-72 are 0.0335 mA cm^{-2} and 0.0244 mA cm^{-2}, respectively. The results show that Pt/CS has a better durability than Pt/XC-72 in 0.5 mol L^{-1} CH_3OH + 0.5 mol L^{-1} H_2SO_4 solution.

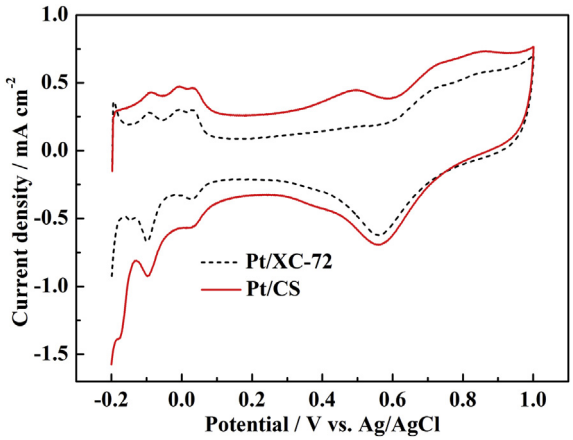

Fig. 9. CVs of Pt/XC-72 and Pt/CS electrocatalysts in 0.5 mol L^{-1} H_2SO_4 at 50 mV s^{-1} at room temperature.

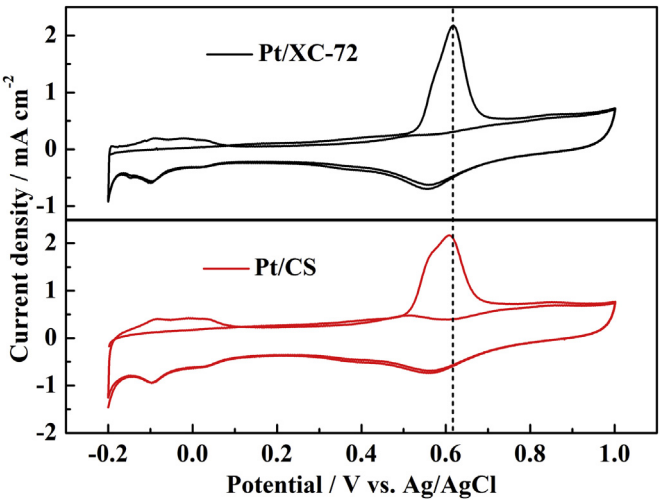

Fig. 10. CO stripping curves of Pt/CS and Pt/XC-72 in 0.5 mol L^{-1} H_2SO_4 at 50 mV s^{-1} at room temperature.

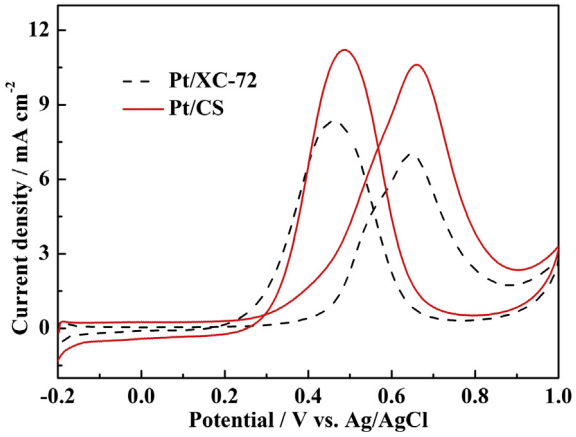

Fig. 11. CV plots of Pt/CS and Pt/XC-72 electrodes in N_2-saturated 0.5 mol L^{-1} H_2SO_4 + 0.5 mol L^{-1} CH_3OH with a scan rate of 50 mV s^{-1} at room temperature.

Tafel plots of ethanol methanol on Pt/CS and Pt/XC-72 derived from the linear sweep voltammograms in N_2-saturated 0.5 mol L^{-1} H_2SO_4 + 0.5 mol L^{-1} CH_3OH aqueous solution are shown in Fig. 13. Tafel plots can be fitted and divided into two linear regions for both

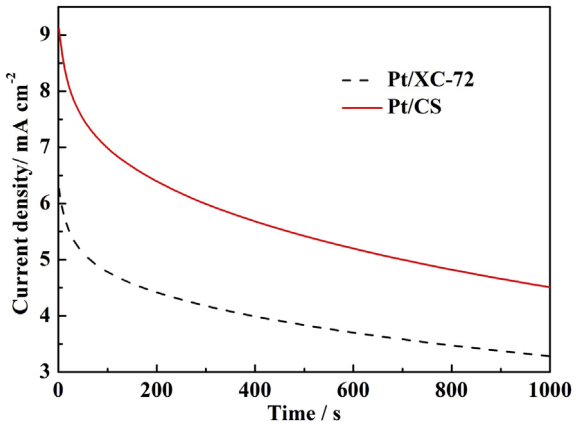

Fig. 12. Chronoamperometric curves of Pt/CS and Pt/XC-72 in N_2-saturated 0.5 mol L^{-1} CH_3OH + 0.5 mol L^{-1} H_2SO_4.

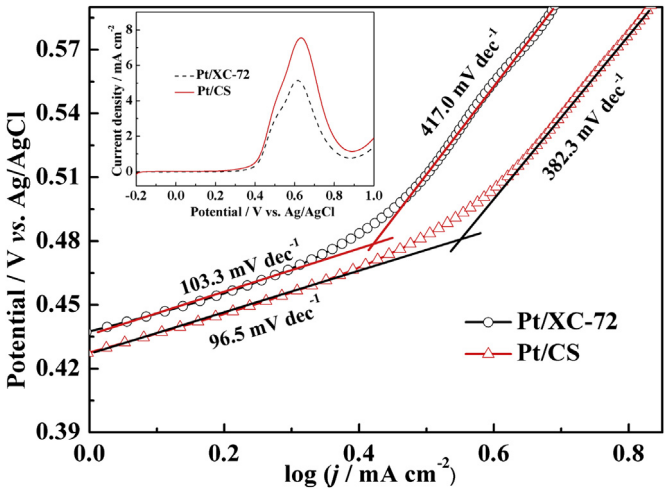

Fig. 13. Tafel plots of Pt/XC-72 and Pt/CS catalysts derived line scan voltammograms (the inset) in N_2-saturated 0.5 mol L^{-1} CH_3OH + 0.5 mol L^{-1} H_2SO_4 solution; scan rate: 5 mV s^{-1}.

two catalysts. The Tafel slopes involve two steps, i.e. alcohol adsorption and dehydrogenation in the low potential range and oxidative removal of CO-like species in the high potential range [38]. The difference of the values of Tafel slopes at low and high potential ranges indicates a possible change of reaction mechanism, or at least a change of rate-determining steps. The value of Tafel slopes of Pt/CS and Pt/XC-72 is 96.5 and 103.3 mV dec^{-1}, respectively in the low potential range, which indicates the step of methanol dehydrogenation reaction on Pt/CS is faster than Pt/XC-72 [39]. A sharp change of Tafel slope indicates that removal of poisonous species becomes the rate-determining processes in methanol oxidation reaction at high potential. The value of Tafel slopes of Pt/CS and Pt/XC-72 is 382.3 and 417.0 mV dec^{-1} at high potential, respectively, showing that the step of removing poisonous species on Pt/CS is faster than that on Pt/XC-72. The Tafel plots further prove that Pt/CS has a better electrochemical activity in methanol reduction reaction than Pt/XC-72.

The above electrochemical results indicate that Pt/CS exhibits efficient electrochemical activity for methanol reduction, which could be attributed to the two aspects: one is the presence of N, which leads to the change of chemical state of Pt related to that of Pt/C and unique morphology of Pt nanoparticles. Pt dendritic particles on CS possess inter-grain boundary regions among the small nanoparticles which could act as active sites [40]. The other is the large BET surface area and mesoporous structure of CS which facilitate the catalyst system in contact with the electrolyte interface.

4. Conclusions

Soybean was successfully used to prepare a low cost and nitrogen-containing carbonaceous support with high surface area and mesoporous structure. Subsequent, Pt nanoparticles were deposited on the as-prepared support. TEM image showed that Pt nano sized dendrites were formed on the surface of CS. Pt/CS showed superior catalytic activity to Pt/XC-72 for methanol oxidation. Compared with conventional carbon support, Pt nanoparticles supported on this mesoporous carbon also showed a higher electrocatalytic activity toward methanol oxidation than that of Pt/XC-72. The Pt nanodendrites on CS were highly active for methanol and CO oxidation, which makes it very promising as a new support material for high performance electrocatalysts used in LTFCs.

Acknowledgments

The authors would like to thank the National Natural Science Foundation of China (21163018, 21363022, and 51362027) for financially supporting this work.

References

[1] M.K. Debe, Nature 486 (2012) 43–51.
[2] A. Hawkes, I. Staffell, D. Brett, N. Brandon, Energy Environ. Sci. 2 (2009) 729–744.
[3] V. Mazumder, Y. Lee, S. Sun, Adv. Funct. Mater. 20 (2010) 1224–1231.
[4] H. Wang, V. Linkov, S. Ji, W. Zhang, Z. Lei, R. Wang, S. Afr. J. Chem. 65 (2012) 69–74.
[5] H. Wang, X. Zhang, R. Wang, S. Ji, W. Wang, Q. Wang, Z. Lei, J. Power Sources 196 (2011) 8000–8003.
[6] L. Chen, H. Guo, T. Fujita, A. Hirata, W. Zhang, A. Inoue, M. Chen, Adv. Funct. Mater. 21 (2011) 4364–4370.
[7] R. Bashyam, P. Zelenay, Nature 443 (2006) 63–66.
[8] T. Chen, Z. Cai, Z. Yang, L. Li, X. Sun, T. Huang, A. Yu, H.G. Kia, H. Peng, Adv. Mater. 23 (2011) 4620–4625.
[9] K. Gong, F. Du, Z. Xia, M. Durstock, L. Dai, Science 323 (2009) 760–764.
[10] R. Wang, Z. Zhang, H. Wang, Z. Lei, Electrochem. Commun. 11 (2009) 1089–1091.
[11] X. Yu, S. Ye, J. Power Sources 172 (2007) 145–154.
[12] Z. Wen, S. Ci, F. Zhang, X. Feng, S. Cui, S. Mao, S. Luo, Z. He, J. Chen, Adv. Mater. 24 (2012) 1399–1404.
[13] D.C. Higgins, D. Meza, Z. Chen, J. Phys. Chem. C 114 (2010) 21982–21988.
[14] C.H. Choi, M.W. Chung, H.C. Kwon, S.H. Park, S.I. Woo, J. Mater. Chem. A 1 (2013) 3694–3699.
[15] D. Chen, L. Tang, J. Li, Chem. Soc. Rev. 39 (2010) 3157–3180.
[16] Y. Zhao, L. Yang, S. Chen, X. Wang, Y. Ma, Q. Wu, Y. Jiang, W. Qian, Z. Hu, J. Am. Chem. Soc. 135 (2013) 1201–1204.
[17] R. Imran Jafri, N. Rajalakshmi, S. Ramaprabhu, J. Mater. Chem. 20 (2010) 7114–7117.
[18] M.L. Anderson, R.M. Stroud, D.R. Rolison, Nano Lett. 2 (2002) 235–240.
[19] E. Antolini, Appl. Catal. B 88 (2009) 1–24.
[20] D. Zhao, J. Feng, Q. Huo, N. Melosh, G.H. Fredrickson, B.F. Chmelka, G.D. Stucky, Science 279 (1998) 548–552.
[21] R.-S. Juang, F.-C. Wu, R.-L. Tseng, Colloids Surf. A 201 (2002) 191–199.
[22] D. Dollimore, G.R. Heal, J. Appl. Chem. 14 (1964) 109–114.
[23] R. Wang, X. Li, H. Li, Q. Wang, H. Wang, W. Wang, J. Kang, Y. Chang, Z. Lei, Int. J. Hydrogen Energy 36 (2011) 5775–5781.
[24] Q.-H. Yang, P.-X. Hou, M. Unno, S. Yamauchi, R. Saito, T. Kyotani, Nano Lett. 5 (2005) 2465–2469.
[25] Z. Chen, D. Higgins, H. Tao, R.S. Hsu, Z. Chen, J. Phys. Chem. C 113 (2009) 21008–21013.
[26] S. Yang, L. Zhi, K. Tang, X. Feng, J. Maier, K. Müllen, Adv. Funct. Mater. 22 (2012) 3634–3640.
[27] K. Ghosh, M. Kumar, T. Maruyama, Y. Ando, Carbon 48 (2010) 191–200.
[28] R. Chetty, S. Kundu, W. Xia, M. Bron, W. Schuhmann, V. Chirila, W. Brandl, T. Reinecke, M. Muhler, Electrochim. Acta 54 (2009) 4208–4215.
[29] H. Wang, H. Da, S. Ji, S. Liao, R. Wang, J. Electrochem Soc. 160 (2013) H266–H270.
[30] M. Oezaslan, F. Hasché, P. Strasser, Chem. Mater. 23 (2011) 2159–2165.
[31] B. Lim, M. Jiang, P.H. Camargo, E.C. Cho, J. Tao, X. Lu, Y. Zhu, Y. Xia, Science 324 (2009) 1302–1305.
[32] C. Roth, M. Goetz, H. Fuess, J. Appl. Electrochem. 31 (2001) 793–798.
[33] F. Su, Z. Tian, C.K. Poh, Z. Wang, S.H. Lim, Z. Liu, J. Lin, Chem. Mater. 22 (2009) 832–839.
[34] J.R. Pels, F. Kapteijn, J.A. Moulijn, Q. Zhu, K.M. Thomas, Carbon 33 (1995) 1641–1653.
[35] S. Shanmugam, T. Osaka, Chem. Commun. 47 (2011) 4463–4465.
[36] B.Y. Xia, J.N. Wang, X.X. Wang, J. Phys. Chem. C 113 (2009) 18115–18120.
[37] T. Zhou, H. Wang, K. Julian, S. Ji, V. Linkov, R. Wang, RSC Adv. 3 (2013) 16949–16953.
[38] Y. Huang, J. Cai, M. Liu, Y. Guo, Electrochim. Acta 83 (2012) 1–6.
[39] W. Wang, Y. Li, H. Wang, React. Kinet. Mech. Cat. 108 (2013) 433–441.
[40] Y. Ma, H. Wang, S. Ji, V. Linkov, R. Wang, J. Power Sources 247 (2014) 142–150.